Supplementary Information for "Measurement of a strong nonlinear force between superconductors compatible with the Casimir force"

Matthijs H. J. de Jong,[1] Evren Korkmazgil,[1] Louise Banniard,[1] Mika A. Sillanpää,[1] and Laure Mercier de Lépinay[1,*]

[1]*Department of Applied Physics, Aalto University, FI-00076 Aalto, Finland*

(Dated: June 8, 2026)

I. SUPPLEMENTARY NOTE

Casimir and van der Waals regimes

Here we justify that the system studied in this work is expected to operate in the force regime commonly referred to as Casimir regime rather than the regime called van der Waals regime. The two regimes are defined for example in Supplementary Ref. 1, which is a seminal work on the topic of the Casimir force by Lifshitz. In the van der Waals regime, the retardation of the response of one object to charge fluctuations in the other object (or electromagnetic fluctuations at the other object, depending on the point of view adopted to describe the force) is negligible. This regime corresponds to small separations. The Casimir regime corresponds to larger separations where the retardation is important. The Lifshitz model for the estimation of dispersion forces (Eq. (5) of the main text) predicts both regimes and allows to define a threshold between the two, as illustrated in Supplementary Fig. 1. In our equation of motion for the mechanics, we use the fitted strength and scaling of the Casimir force that is shown by the dotted line in Supplementary Fig. 1. The van der Waals regime appears at separations of $1-3$ nm nanometers, much smaller than separations considered here.

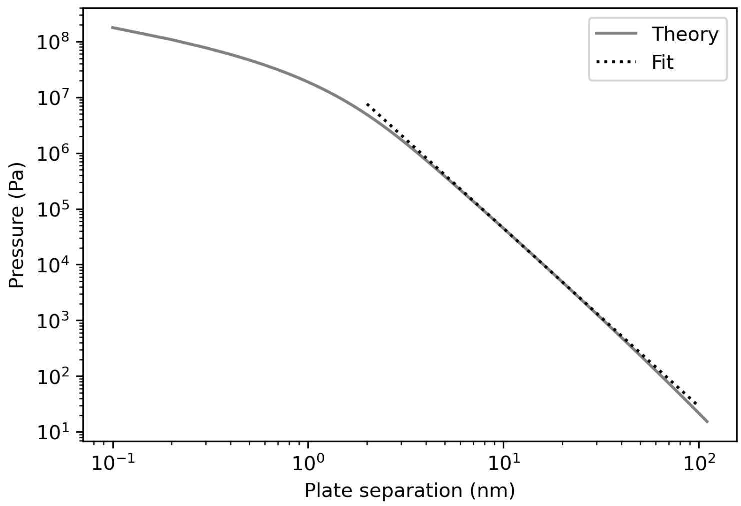

Supplementary Fig. 1 | Calculation of the pressure across a large range of distances in the Lifshitz formalism. The dotted line shows the Casimir force expression used in the main text, and it is plotted over a large range of separations of the order of magnitude expected in the device $2-100$ nm.

In Supplementary Ref. 2, it was shown that the effective threshold of distance between realistic surfaces (e.g., with non-negligible roughness) that separate the van der Waals and the Casimir regimes is of the order of 10% of the plasma wavelength. For aluminium, this crossover is then expected around 9.5 nm. Although this is closer to the experimental separation estimated from the model of force employed in the paper, it is still inferior, and the van der Waals regime has to be understood as a limit case (for separations much smaller than the threshold). Therefore, in the experimental situation explored in this paper, we refer to the Casimir force.

* laure.mercierdelepinay@aalto.fi

II. SUPPLEMENTARY METHODS

A. Optomechanical description

1. *Equations of motion*

At small amplitude of displacement around the equilibrium position shifted by the nonlinear potential, the optomechanical equations of motion are[3]:

$$\begin{aligned} \dot{\tilde{x}}(t) &= \omega_\mathrm{m} p, \\ \dot{p}(t) &= -\omega_\mathrm{m}\tilde{x} - \gamma_\mathrm{m} p - g_0 |a|^2, \\ \dot{a}(t) &= -(i\Delta + \kappa/2)a + i g_0 \tilde{x} a + \sqrt{\kappa_\mathrm{e}}\, s_\mathrm{in}(t) \end{aligned} \tag{1}$$

The displacement and momentum are respectively denoted $\tilde{x}$ and p, and a denotes the cavity mode field complex amplitude. The mechanical parameters ω_m, γ_m, the cavity parameters κ, Δ, and the coupling strength g_0 are the same as in the main text and their values are listed in Table I. Note that we use the mechanical parameters ω_m and γ_m which are the 'dressed' parameters from the Casimir force rather than the 'unperturbed' parameters ω_r and γ_r. We operate in a frame rotating at the frequency of the microwave drive. Our system is strongly driven, so we can safely neglect the noise terms in the numerical simulations and use a classical formalism. The input field is a combination of the (strong) drive at the cavity frequency, and a weaker sideband drive. It can be expressed in the rotating frame as

$$s_\mathrm{in}(t) = \sqrt{P_\mathrm{mw}/\hbar\omega_\mathrm{c}} + \sqrt{P_\mathrm{sb}/\hbar\omega_\mathrm{c}}\, e^{-i\omega_\mathrm{m} t}. \tag{2}$$

This is enough to solve the system of equations of motion for some initial conditions $\tilde{x}(0)$, $p(0)$, and $a(0)$. We model the detected signal using input-output theory

$$a_\mathrm{out} = \sqrt{\kappa_\mathrm{e}}\, a - s_\mathrm{in}. \tag{3}$$

The spectrum of the output field is given by the Fourier transform $\mathcal{F}$,

$$S_\mathrm{out}(\omega) = \left|\mathcal{F}\left\{(a_\mathrm{out} + a^*_\mathrm{out})/2\right\}\right|^2. \tag{4}$$

This spectrum $S_\mathrm{out}(\omega)$ is recorded with a spectrum analyzer.

We can independently calibrate the parameters ω_m, γ_m, κ, Δ, and g_0 as reported in Supplementary Method C. We also accurately know the powers of the cavity and sideband drive tones we send in, but between the output of the generators and the cavity are attenuators and cable losses (see Methods in the main text). To calibrate the amplitudes of our drives at the cavity entrance, we first make a crude estimation based on the relative sideband powers (next section), and then refine it using Eq. 4 (section after that).

2. *Relative sideband powers*

We have recorded the powers of six sidebands ($\pm\omega_m$, $\pm 2\omega_\mathrm{m}$, and $\pm 3\omega_\mathrm{m}$) for the measurements reported in the main text. We can compare the relative powers of each of the sidebands, and compare the powers with the sideband drive, to show how our detected signal is proportional to the mechanical displacement. We use the perturbative treatment of the classical coupled mode equations[3,4]. Our starting point is a simplified version of Eqs. (60) and (61) of Supplementary Ref. 3, where the steady state cavity field amplitude a_0 is defined by the input power of the microwave drive at the cavity frequency, a_mw, and cavity parameters κ_e, Δ and κ. We define x_amp as a quadrature of the mechanical signal and choose the origin of times such that $\tilde{x} = x_\mathrm{amp}(t)\sin(\omega_m t)$.

$$\begin{aligned} a_0 &= a_\mathrm{mw} \frac{\sqrt{\kappa_\mathrm{e}}}{-i\Delta + \kappa/2} \\ a_{+1} &= \frac{g_0 x_\mathrm{amp}}{2 x_\mathrm{zpf}} \frac{a_0}{-i(\Delta + \omega_\mathrm{m}) + \kappa/2} \\ a_{-1} &= \frac{g_0 x_\mathrm{amp}}{2 x_\mathrm{zpf}} \frac{a_0}{-i(\Delta - \omega_\mathrm{m}) + \kappa/2}. \end{aligned} \tag{5}$$

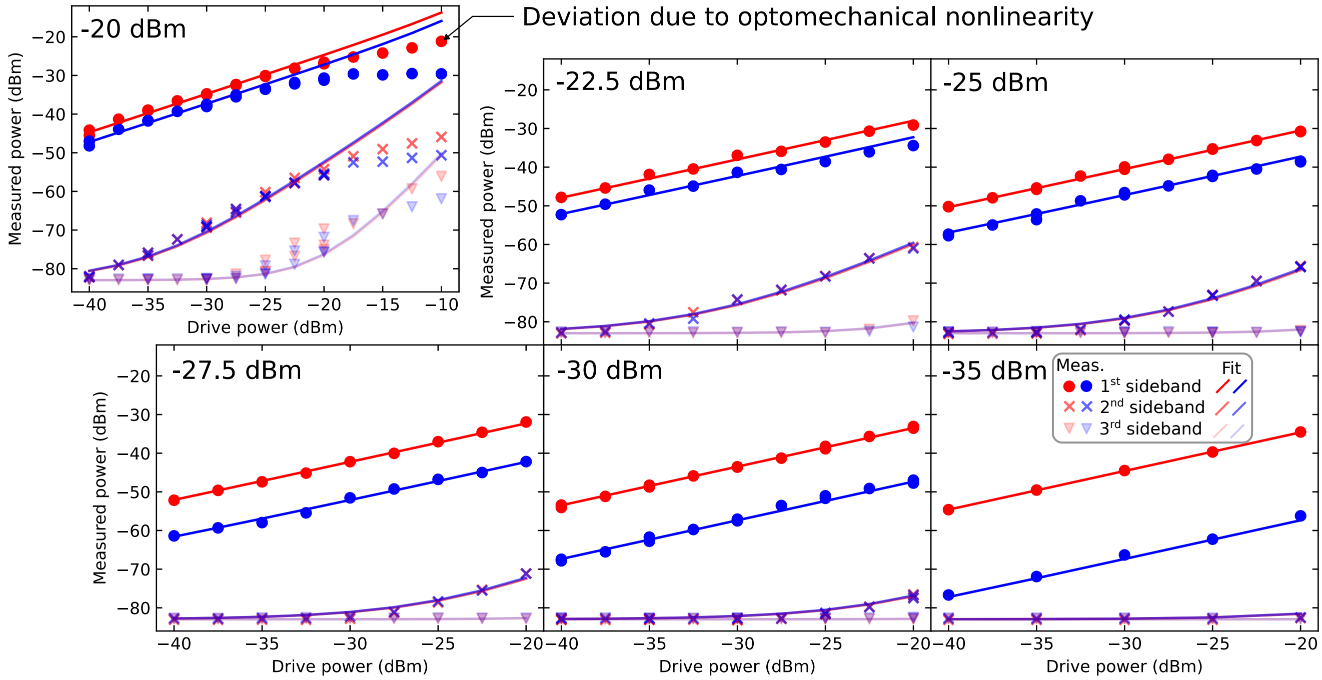

Supplementary Fig. 2 | Relative sideband powers. Comparison of the maximum powers in all 6 sidebands for different powers of cavity drive a_{mw} (panel labels) and sideband drive a_{sb} (x-axis). The colors indicate whether the sideband is on the red side of the cavity ($a_{-1,-2,-3}$) or on the blue side ($a_{+1,+2,+3}$). The symbols are measurement points, solid lines are fits to the model of Eq. (10). Only at the highest powers does our model deviate from the data, which is due to the optomechanical nonlinearity. The asymmetry of the first-order sidebands provides a power reference between the applied drives. The higher order sidebands are symmetric, so they overlap and appear purple in the plot. This symmetry motivates neglecting the scattering processes of a_{sb} which we have done in constructing Eq. (3) of the main text.

Here, the amplitude of the anti-Stokes- and Stokes-scattered sidebands are denoted with a_{+1} and a_{-1} respectively. These exist in the spectrum at $\pm\omega_{\mathrm{m}}$ away from the frequency of a_0, and they are related to the mechanical amplitude x_{amp}. This expansion is valid regardless of the spectrum of x_{amp}, and simply requires that it is peaked close to 0 frequency and sufficiently narrow so that the sidebands are well-separated.

Our six-sideband treatment is based on repeating the treatment of Eq. (5), but considering $a_{\pm 1,2,3}$ as the source term instead of a_0. That is, from a_{+1} we recognize two scattering processes, which end up at a_0 and a_{+2} respectively.

$$
\begin{aligned}
a_0 &= +\frac{g_0 x_{\mathrm{amp}}}{2x_{\mathrm{zpf}}}\frac{a_{+1}}{-i\Delta+\kappa/2} \\
a_{+2} &= \frac{g_0 x_{\mathrm{amp}}}{2x_{\mathrm{zpf}}}\frac{a_{+1}}{-i(\Delta+2\omega_{\mathrm{m}})+\kappa/2}
\end{aligned}
\tag{6}
$$

By repeating this treatment for all orders of sidebands that we measure, we gain a set of linear coupled equations. This resulting system can be written in matrix form as

$$
\begin{bmatrix}
1 & d_{+3} & 0 & 0 & 0 & 0 & 0 \\
d_{+2} & 1 & d_{+2} & 0 & 0 & 0 & 0 \\
0 & d_{+1} & 1 & d_{+1} & 0 & 0 & 0 \\
0 & 0 & d_0 & 1 & d_0 & 0 & 0 \\
0 & 0 & 0 & d_{-1} & 1 & d_{-1} & 0 \\
0 & 0 & 0 & 0 & d_{-2} & 1 & d_{-2} \\
0 & 0 & 0 & 0 & 0 & d_{-3} & 1
\end{bmatrix}
\begin{bmatrix}
a_{+3} \\ a_{+2} \\ a_{+1} \\ a_0 \\ a_{-1} \\ a_{-2} \\ a_{-3}
\end{bmatrix}
=
\begin{bmatrix}
0 \\ 0 \\ 0 \\ \frac{a_{\mathrm{mw}}\sqrt{\kappa_{\mathrm{e}}}}{-i\Delta+\kappa/2} \\ 0 \\ 0 \\ 0
\end{bmatrix}
\tag{7}
$$

with

$$
d_{\pm n} = \frac{g_0 x_{\mathrm{amp}}}{2x_{\mathrm{zpf}}}\frac{1}{-i(\Delta\pm n\omega_{\mathrm{m}})+\kappa/2}.
\tag{8}
$$

We have made the simplifying assumption that repeated interactions ending up at lower-order sideband are negligible in power compared to the (original) lower-order sideband power. This is a valid assumption when $g_0 \ll \kappa/2$, since each individual photon is much more likely to exit the cavity than to scatter from the mechanical resonator.

It is fairly straightforward to numerically solve Eq. (7) using e.g., Python. This model is valid when the optomechanical interaction is dominated by a single drive tone, which in our case is a_{mw}. However, we have a weaker second drive, a_{sb}, at $-\omega_{\mathrm{m}}$. Since it is much weaker than a_{mw}, we neglect the effect of any scattering interactions from a_{sb} on the sideband amplitudes. The result of this is that there is an asymmetry only between the first-order red (a_{-1}) and blue (a_{+1}) sidebands. If we had included the scattering interactions of the weaker drive, the red and blue sidebands of all orders would have the same asymmetry. However, from the measurements we will see that this is not the case (only the first order sidebands are asymmetric), and therefore we neglect the scattering interactions of a_{sb} in our sideband amplitude calculation. Thus the resulting amplitude(s) due to this drive are

$$\vec{a}_{\mathrm{sb}} = \begin{bmatrix} 0 \\ 0 \\ 0 \\ 0 \\ \frac{a_{\mathrm{sb}}\sqrt{\kappa_{\mathrm{e}}}}{(-i(\Delta-\omega_{\mathrm{m}})+\kappa/2)} \\ 0 \\ 0 \end{bmatrix}. \tag{9}$$

To fit this model to our data, we solve Eq. (7) for $\vec{a}$ and compute the output field using the input-output formalism. Here we also add the solution for the weaker drive field a_{sb}. The output field is described by

$$a_{\mathrm{out}} = \sqrt{\kappa_{\mathrm{e}}}(\vec{a} + \vec{a}_{\mathrm{sb}}) - \begin{bmatrix} 0 \\ 0 \\ 0 \\ \frac{a_{\mathrm{mw}}}{-i\Delta+\kappa/2} \\ \frac{a_{\mathrm{sb}}}{-i(\Delta-\omega_{\mathrm{m}})+\kappa/2} \\ 0 \\ 0 \end{bmatrix} \tag{10}$$

In Supplementary Fig. 2 we have plotted the maximum observed powers of each of our measured sidebands (markers) for different drive powers, and compared those to our fitted model (solid lines). There is an excellent agreement at all but the highest powers. For the highest powers, the optomechanical nonlinearity reduces the drive efficiency, which reduces the maximum powers seen in the sidebands.

The measurements record the sideband powers, and from our model we extract $|a_{\mathrm{out}}|^2$, but we need two conversion factors to link the theory to our experiments (one for each axis of Supplementary Fig. 2). There is also attenuation from the room-temperature source to the cavity at 10 mK (see Methods), which gives us an additional conversion factor. The simplifications of the model of Eq. (7) are not ideal to use it as an accurate calibration tool between mechanical amplitude and measured power, but it serves as a quick estimation of these conversion factors. We use these as an initial guess for the simulation-based calibration method using the optomechanical equations of motion described in the next section.

3. *Absolute amplitude calibration*

Here we describe the calibration of measured signals into displacement. After the calibration of optomechanical parameters described in Supplementary Method C, a remaining unknown is the total attenuation between microwave sources and the cavity entrance. Indeed, input lines include attenuators with known attenuation (see Fig. 6 of Methods) but also losses incurred along the cables whose exact value is unknown. To realize this calibration, we compare the measured response of the system at small displacements with numerical predictions.

To model the response, we let Eq. (1) evolve numerically until it has settled into a steady state, and simulate the steady state for an additional 10 ms. We compute the Fourier transform of the output field, as in Eq. (4), which gives us the observed power, while we obtain the mechanical oscillation amplitude from the size of the orbit of $\tilde{x}$ of Eq. (1). To scale the simulated signal in the same way as the measured signal, we multiply the simulation result by the detection scale factor (W/photon) S_{c} found in Supplementary Method C and compensate for the finite simulation time. We then compare the maximum simulated power around the first red and the first blue sideband ($\omega_c \pm \omega_m$) with the maximum measured amplitude. We calibrate the cables attenuation by matching the computed and measured signals simultaneously for these two sidebands' maxima (see Supplementary Fig. 3)

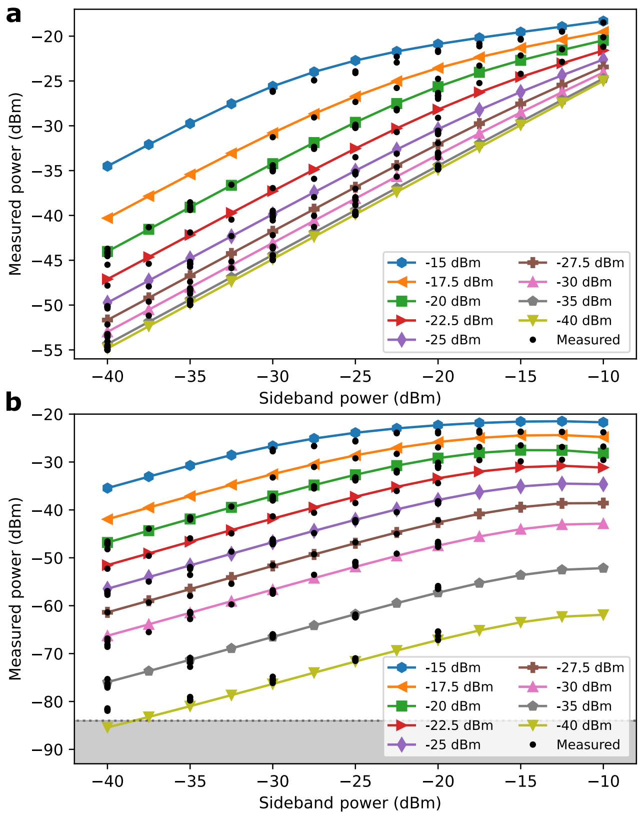

Supplementary Fig. 3 | Sideband calibration. **a** Simulated powers (colored lines with various markers) and observed peak powers (black dots) for the red sideband. The legend indicates P_{mw}, the x-axis is P_{sb}. The agreement between the simulations and the measurements at low power serves as a calibration for the numerical simulations. **b** Idem, but for the blue sideband. The grey shaded area shows the noise floor for the measurements.

as well as for a point on the side of the red sideband detuned by 3 kHz (see Supplementary Fig. 4). Supplementary Fig. 3 shows that the calibrated values allow to match data and simulations for all combinations where both powers are in the range $[-40\,\mathrm{dB}, -30\,\mathrm{dB}]$: these powers correspond to those for which the mechanical responses were measured to be approximately Lorentzian and therefore reasonably well described by Eq. (1). Additionally, Supplementary Fig. 4 shows that the same calibrated values allow to match data and simulations at all powers for the off-resonant point where the displacement is also very small.

From this procedure, we find that the power of the cavity drive P_{mw} at the input of the device is attenuated by 47.4 dB from the power issued by the generator. Out of this attenuation, 36 dB comes from the installed attenuators shown in Fig. 6 of Methods, 3 dB comes from a splitter at room temperature, and the rest (about 8 dB) is of the order of magnitude of the total attenuation expected from the cryogenic transmission line itself. Similarly, we find that the sideband tone power P_{sb} at the input of the cavity is attenuated by 69.6 dB from the power issued by the generator. The difference of 22.2 dB between the attenuations of the two tones is mainly due to the 20 dB attenuation of a directional coupler in front of the vector network analyzer generating the sideband drive (see Fig. 6 of Methods).

Supplementary Fig. 3 also shows the maximum amplitude of sidebands computed at larger drives. As shown in the figure, while Eq. (1) cannot reproduce the asymmetric mechanical lineshapes measured at larger drives, its solution still predicts the *maximum amplitude* of measured sidebands rather accurately up to very large driving forces.

The displacement amplitude simulated for all combinations of cavity and sideband drive powers are shown in Supplementary Fig. 5. At small amplitudes, the maximum amplitude scales linearly with both cavity and sideband drive powers, but at some point this relation breaks down. This is not due to the nonlinearity of the oscillator since Eq. (1) does not simulate it. Instead, this is due to the loss of drive efficiency due to optomechanical effects.

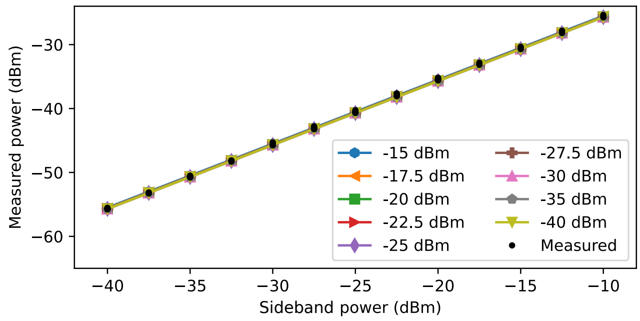

Supplementary Fig. 4 | Input power calibration. The 3 kHz off-resonant drive simulations show a perfect overlap between all simulated (colored markers) and measured powers (black dots).

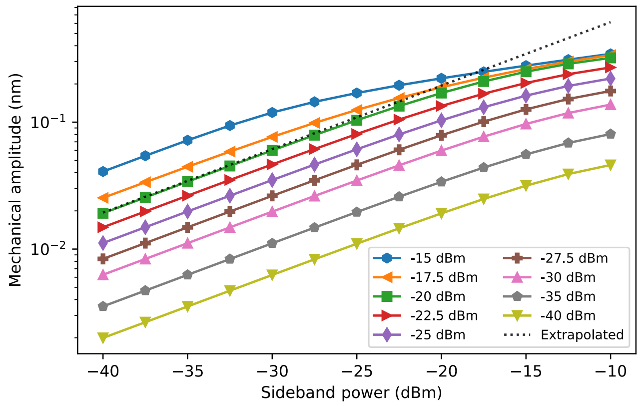

Supplementary Fig. 5 | Mechanical amplitudes simulated with 1 for different combinations of cavity and sideband drive powers.

4. *Calculation of the drive efficiency*

The tenet of (dispersive) cavity optomechanics is that the cavity frequency ω_c shifts as a result of the displacement $\tilde{x}$[3]. In this work, the amplitude of $\tilde{x}$ is significant, and the cavity frequency shift $\frac{\partial \omega_c}{\partial \tilde{x}}$ causes a mismatch between the cavity frequency and the drive frequencies, $\omega_{mw} \simeq \omega_c$ and $\omega_{sb} \simeq \omega_c - \omega_m$. The cavity frequency $\omega_c(t)$ is thus a function of time, it oscillates at ω_m depending on the exact trajectory of the drum. For larger oscillations of $\tilde{x}$, the frequency mismatch between cavity and drive is greater and the power in the cavity decreases. The oscillation is fast with respect to the cavity linewidth, as we are in the resolved sideband limit $\kappa \ll \omega_m$, which means that the cavity amplitude changes slowly with respect to the oscillation of ω_m. Furthermore, we also have two drives separated in frequency. So while the power resulting from the drive at ω_c is maximal for small amplitudes of $\tilde{x}$, the power resulting from the drive at $\omega_c - \omega_m$ peaks for some specific oscillation amplitude of $\tilde{x}$.

We calculate the drive efficiency by solving Eq. (1) with a fixed mechanical amplitude x. We let the system simulate only for a brief time, such that the cavity amplitude a has had time to stabilize. From the last 20 mechanical periods, we extract the power in the cavity. This brief simulation is repeated for 101 values of x logarithmically spaced between 1 pm and 1 nm for all different cavity drive powers used in the experiments.

In the regime that is relevant for our experiment, the drive efficiency is 1 for small mechanical amplitudes (< 100 pm), and decreases quickly towards zero beyond that. However, at even larger mechanical amplitudes, beyond what we achieve in this work, the drive efficiency recovers to a non-negligible number in a series of bands that represent stable orbits as described in Supplementary Ref. 5.

To fit a measured response driven by a given combination of powers, we first estimate the driving force F_0 (unaffected by the loss of drive efficiency) corresponding to that combination using the calibration detailed in the previous section. We simulate the corresponding response using MatCont as described in Methods, then correct it point-by-point to account for the loss of drive efficiency. This procedure is repeated for different values of parameter d appearing in the Casimir force model in order to realize the fit using a standard least-square routine.

B. Simulating the Casimir nonlinearity

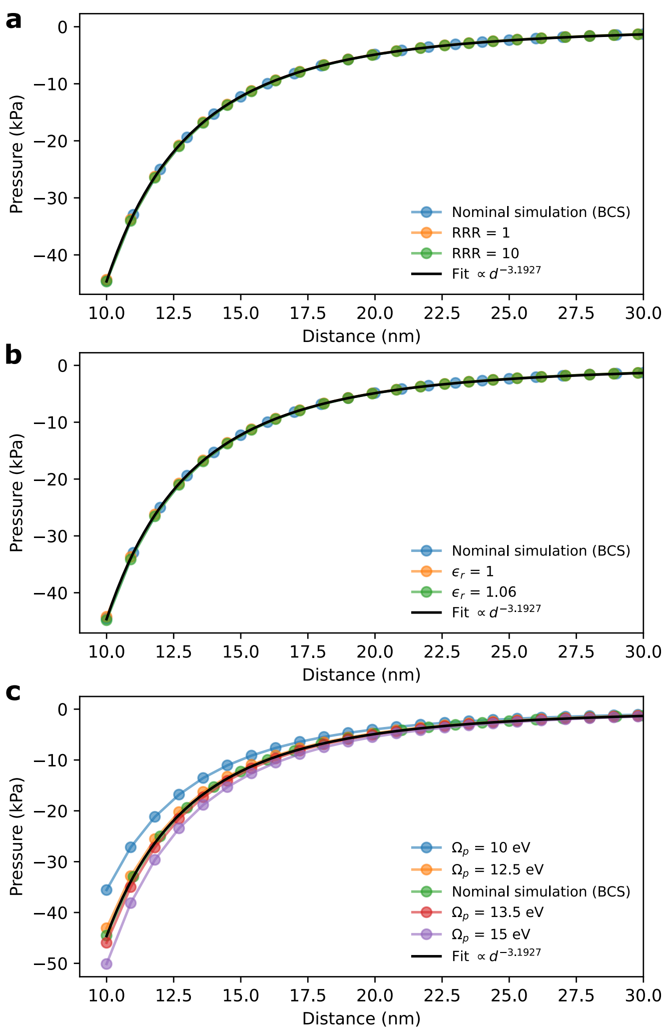

Supplementary Fig. 6 | Effect of material parameters. **a** The residual resistance ratio (RRR) rescales the dissipation rate $\gamma_\mathrm{p} = \gamma_0/\mathrm{RRR}$, but varying it from the nominal value RRR = 2 does not significantly affect the Casimir pressure. **b** Varying the relative permittivity of aluminium from the the nominal value $\epsilon_\mathrm{r} = 1.03$ does not significantly affect the Casimir pressure. **c** Varying the plasma frequency from the nominal value $\Omega_\mathrm{p} = 13$ eV affect the Casimir pressure amplitude P more strongly than the Casimir scaling n.

1. Role of Casimir parameters

We perform the fit of distance d without considering variations in the calculated Casimir pressure, i.e., we consider the Casimir pressure amplitude P and scaling n to be fixed. To motivate this choice, we show that the Casimir pressure does not vary much with the material parameters γ_0 (or RRR), ϵ_0, and Ω_p. We repeat the Casimir pressure calculations for different material parameters, as shown in Supplementary Fig. 6, and we fit curves of the form $P_\mathrm{c} = P/d^n$ to distinguish changes in the amplitude of the Casimir pressure (P) from changes in the Casimir scaling (n).

The residual resistivity ratio RRR can vary depending on the material source and deposition method. We have previously measured similar films to have RRR = 2 using a four-point probe method. Variations in the RRR affect the phenomenological dissipation rate, $\gamma_\mathrm{p} = \gamma_0/\mathrm{RRR}$, so Supplementary Fig. 6a shows the effect of varying either RRR or γ_0. From the overlap between the curves, we conclude that RRR and γ_0 affect neither the Casimir pressure amplitude P nor exponent n.

The relative permittivity of aluminium, $\epsilon_\mathrm{r} = 1.03$ was experimentally determined and follows from the core-interband transitions of the aluminium atoms[6]. We show in Supplementary Fig. 6 that variations in this parameter do not lead to significant changes in the Casimir pressure.

We take the plasma frequency of aluminium $\Omega_p = 13$ eV from Supplementary Ref. 6. In Supplementary Fig. 6 we show that varying Ω_p changes the Casimir pressure, but its effect on the Casimir scaling is marginal. A 25% variation in Ω_p corresponds to a 25% variation in P, but less than 1% variation in n.

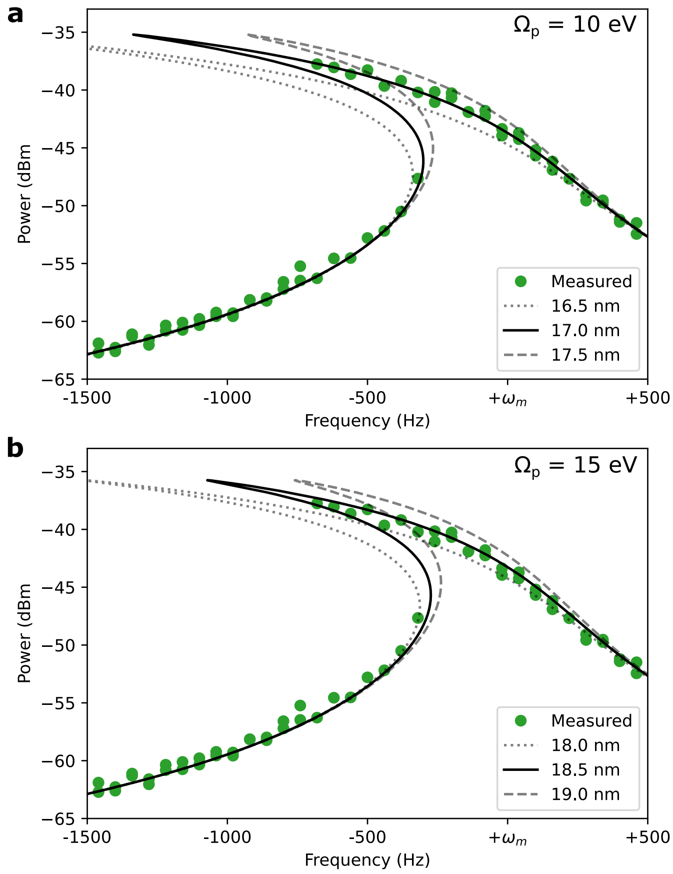

Supplementary Fig. 7 | Fits for Casimir force variations. a The Casimir force for a material with plasma frequency $\omega_p = 10$ eV is weaker than the nominal Casimir force used in this work. The Casimir nonlinearity fits to a plate separation of $d = 17.00 \pm 0.25$ nm. **b** The Casimir force for a material with plasma frequency $\omega_p = 15$ eV fits to a plate separation of $d = 18.50 \pm 0.25$ nm.

To further motivate our choice to consider the calculated Casimir parameters as fixed values, we fit our experimental data to the Casimir force calculated with $\Omega_p = 10$ and 15 eV. The results are shown in Supplementary Fig. 7, where we have taken the optomechanical calibration of mechanical amplitude to be fixed. Taking $\Omega_p = 10$ eV (Supplementary Fig. 7a), the Casimir force is weaker, which means that to experience the same nonlinearity at fixed mechanical amplitude, the plate separation d must be reduced. Vice versa, taking $\Omega_p = 15$ eV (Supplementary Fig. 7b) leads to a better fit at larger d. The variations in Ω_p are significant (25% of the total value), and well beyond the uncertainty of which the plasma frequency is established in aluminium, yet the effect on the fitted parameter d is limited ($\sim$1 nm). Thus, we conclude that our choice to take the Casimir pressure amplitude and scaling to be fixed values leads to a smaller error than the optomechanical amplitude calibration does.

2. *Static shift of frequency and position*

As we illustrated in Fig. 1a of the main text, we start with a harmonic oscillator centered at distance d from the other plate with unperturbed resonance frequency ω_r. The Casimir force pulls the top plate closer to the bottom plate, such that it oscillates around some value $d' < d$, and softens the spring so the mechanical frequency is decreased, $\omega_m < \omega_r$. We do not know d or ω_r a priori, but we can measure ω_m with great accuracy, leaving us to consider d (or somewhat equivalently the Casimir pressure P_c) as a parameter to be fitted. That means that for every value d, we have to find the value of the unperturbed frequency ω_r such that the perturbed frequency $\omega_m = 2\pi \times 10.001$ MHz. Rather than finding a clever algorithm to compute the correct values of ω_r, we numerically evaluate the problem for a selection of d-values and interpolate. In Supplementary Fig. 8 we show the frequencies ω_r that result in the correct value of ω_m for different values of d.

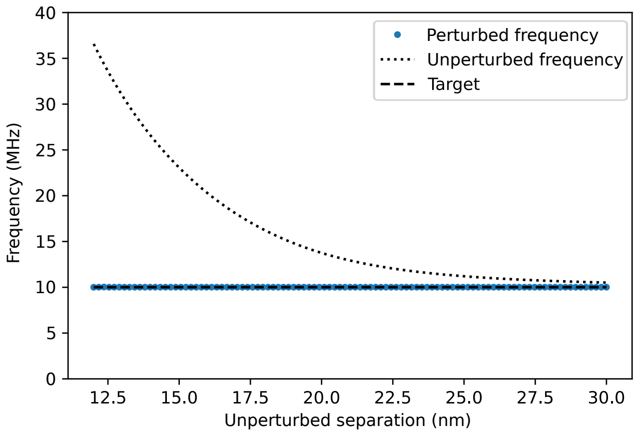

Supplementary Fig. 8 | Casimir frequency shift. Plot of the unperturbed frequencies ω_r for various values of spacing d that result in the correct value for ω_m when the Casimir force is included.

The numerical simulations of the Casimir oscillator in MatCont start with the drive frequency far detuned. To start the continuation, we need this step to converge to a solution. However, the total potential sketched in Fig. 1a of the main text has a local minimum (where our resonator is) and a global minimum beyond the pull-in point. We need to feed MatCont the correct initial values such that it converges to the local minimum instead of showing us the pull-in collapse. To find these, we compute the position of the local minimum of the total potential for various values of d, while using the values of ω_r from Supplementary Fig. 8. The unperturbed frequency ω_r is related to the mechanical stiffness needed to compute the potential, not ω_m. We plot the stable position of the local minimum for different values of d in Supplementary Fig. 9. As with the unperturbed frequencies, we interpolate linearly between the calculated values for the numerical simulations and fits of the main text.

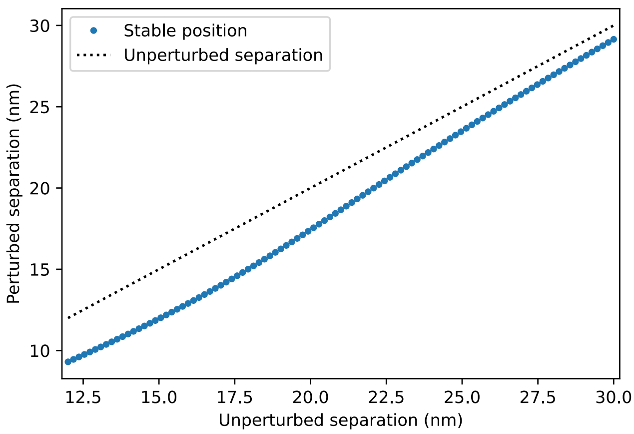

Supplementary Fig. 9 | Shift of the local potential minimum due to the Casimir force. Distance between the local minimum (stable position) and the bottom plate for various values of the unperturbed separation d. The dotted line indicates where the initial separation would be the stable position. For $d = 18.0$ nm, the difference between the unperturbed separation and the local minimum is 2.9 nm.

3. *Role of mechanical parameters*

We study the effect of variations of the parameters of the Casimir effect through numerical simulations. We vary the drive force amplitude F_d, damping coefficient γ_r, separation distance d, and the Casimir exponent n. The results are shown in Supplementary Fig. 10.

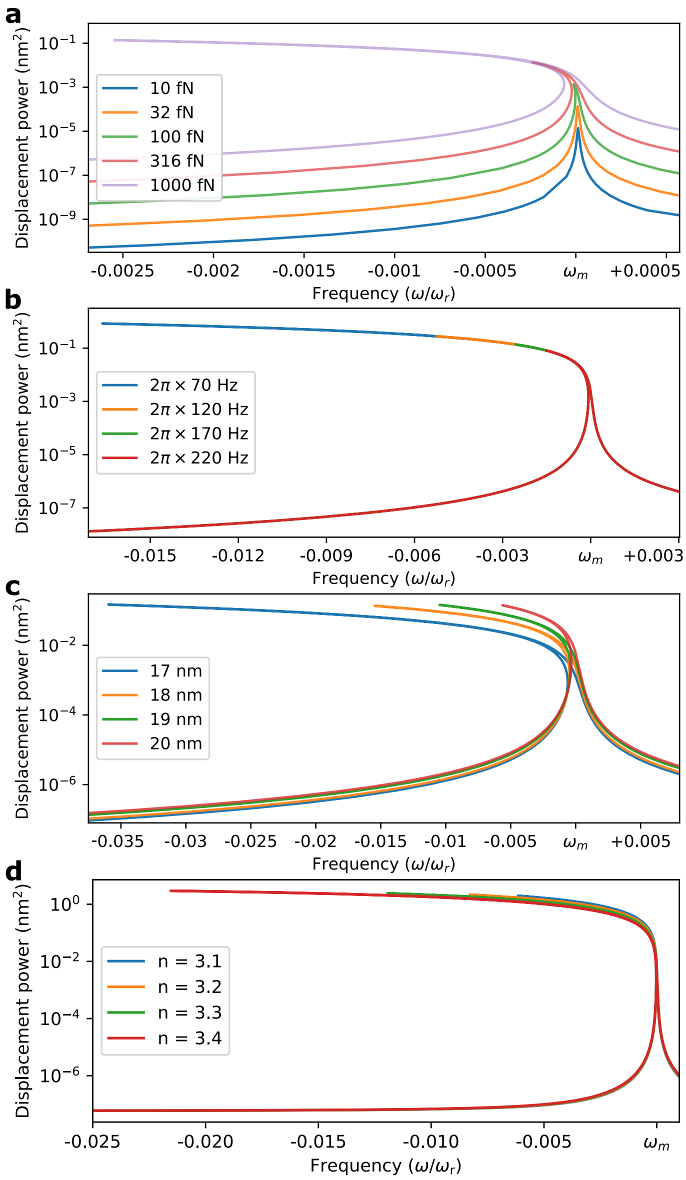

Supplementary Fig. 10 | Effect of the Casimir force parameters. **a** Effect of different drive force amplitudes F_d. **b** Effect of varying the damping coefficient γ_r. **c** Effect of varying the distance between the plates at mechanical zero. d. The frequencies of the curves have been shifted to align on ω_m. **d** Effect of varying the Casimir scaling n, where the amplitude of the Casimir pressure has been fixed at the equilibrium position d'.

We show how the system response transforms from linear behavior at small amplitude to nonlinear behavior at large amplitude in Supplementary Fig. 10a. When the drive force amplitude is small, $F_d = 10$ fN, the frequency response of the system is Lorentzian, as expected. For larger amplitudes, the resonance peak broadens and becomes asymmetrical, indicative of nonlinear resonance where the response of the system is no longer linearly proportional to the drive force. The resonance frequency decreases with increasing amplitude, which indicates that the Casimir force is a strong softening nonlinearity.

In Supplementary Fig. 10b, we study the effect of the mechanical damping rate γ_r. Lower damping allows for greater energy accumulation within the system at equal drive amplitudes, leading to larger oscillations and a more pronounced nonlinearity. However, all the backbones of the curves for different damping rates align, meaning the damping coefficient does not have a significant effect on the nonlinearity we observe.

The most important parameter for Casimir experiments is the separation distance d, which is the distance between the plates in the absence of the Casimir force. Since the Casimir effect strongly scales with the distance d, the Casimir force between drums spaced $d = 17$ nm apart (blue curve in Supplementary Fig. 10c) causes a much stronger nonlinear behavior than for drums spaced $d = 18$ nm apart. The region where there are multiple solutions is much more extended, even if the amplitude of the mechanical oscillations remains the same. All curves were generated using the same drive force, which indicates that the separation distance d does not affect the mechanical amplitude significantly.

Finally, we show the effect of the Casimir force exponent n in Supplementary Fig. 10d. The The Casimir pressure was adjusted for each n such that the value at the equilibrium position (d') was kept constant. While the trend from the change in n somewhat resembles the trend from the change in d, it is noticeable that the peaks curve more sharply with increasing n, while they start curving at lower amplitude for lower d.

C. Characterization of optomechanical system

1. Calibration of microwave cavity parameters

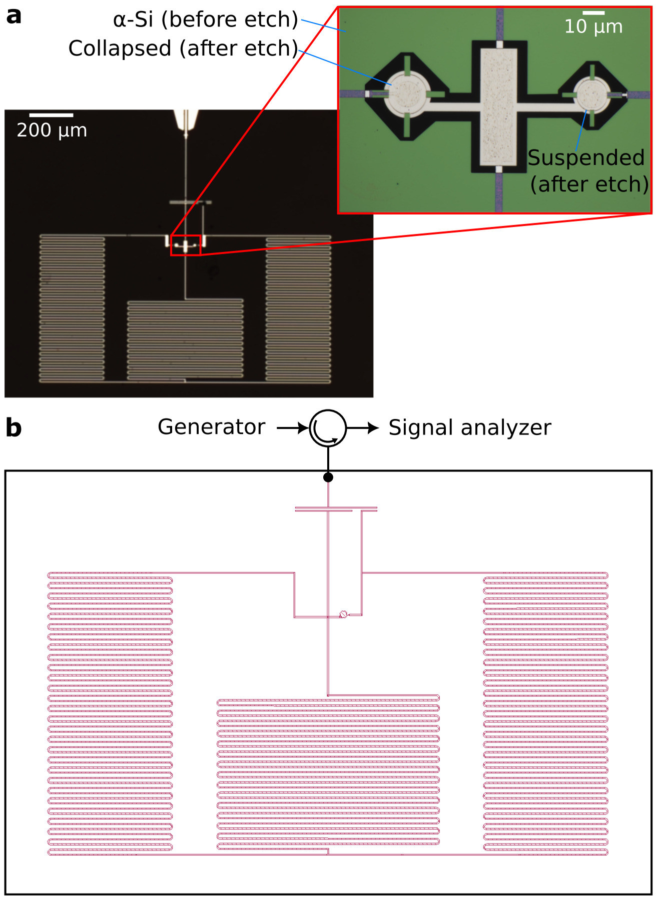

Supplementary Fig. 11 | Microwave cavity. a Microscope image of our microwave cavity (after the experiment), with the inset showing the drums (during fabrication). The larger (left) drum collapsed before the experiment, while the smaller (right) drum survived. **b** Sonnet simulation of our cavity, with the collapsed drum replaced by a short.

Our microwave cavity design was optimized to allow coupling to two separate drum resonators with two cavity modes, as shown in Supplementary Fig. 11a, and described in more detail in the Supplementary of Supplementary Ref. 7. In our device, one of the drum resonators inadvertently collapsed and shorted one half of the cavity, though this cannot be seen in the microscope image. Instead, we deduce this by the number of microwave modes we see (one), its frequency ($\omega_c = 2\pi \times 5.46180$ GHz), and the number of mechanical signals we can observe in a wide-band frequency sweep at high red-sideband drive power (one).

We simulate our cavity using Sonnet, where we have replaced the collapsed drum by a short (Supplementary Fig. 11b). At first, we replace the suspended drum by a numerical capacitance. An initial guess for the capacitance of this drum based on the diameter $2r = 11.3$ μm and a gap of 15.1 nm is 0.059 pF. To provide an initial estimate of the optomechanical coupling, we vary the spacing of the vacuum layer in our Sonnet model, and re-compute the cavity resonance frequency. We find $\frac{\Delta\omega_c}{\Delta x} \simeq$

$2\pi \times 104\ \mathrm{MHz\,nm^{-1}}$. We use the zero point motion $x_{\mathrm{zpf}} = \sqrt{\frac{\hbar}{2m_{\mathrm{eff}}\omega_{\mathrm{m}}}} = 4.6$ fm and estimate the coupling rate $g_0 \simeq x_{\mathrm{xpf}} \frac{\Delta\omega_{\mathrm{c}}}{\Delta x} \simeq 2\pi\times 480$ Hz. This is larger than the coupling rate that we find when we calibrate our system by about a factor 3, which we attribute to details not captured by our simulation: microscopic defects or fabrication imperfections, wire bonds, and box resonances. The simulated microwave cavity mode is not qualitatively affected by these limitations, but the we should treat the optomechanical coupling it yields as an optimistic estimate.

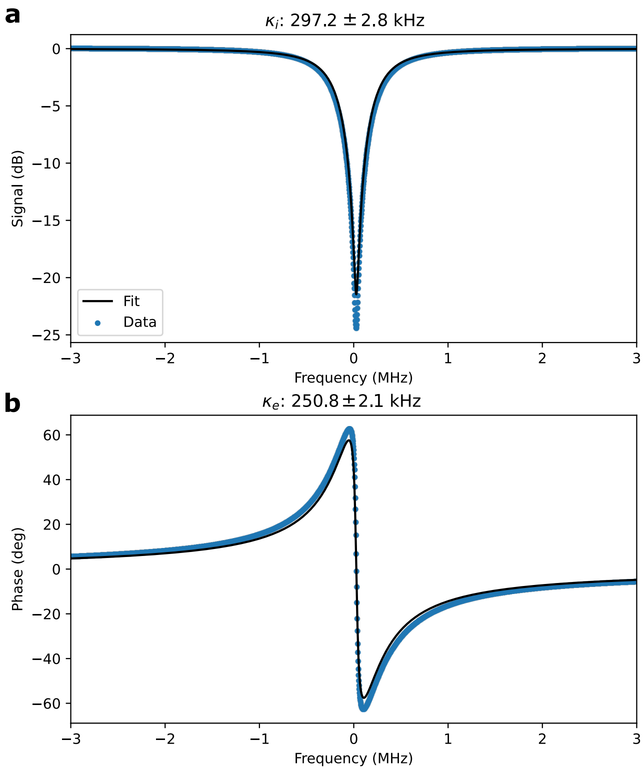

Supplementary Fig. 12 | Microwave cavity calibration. a Amplitude response of the microwave cavity (blue) and the fitted linewidth (black). **b** Phase response of the microwave cavity (blue) and the fitted response (black). The internal and external linewidths, $\kappa_{\mathrm{i}} = 297.2 \pm 2.8$ kHz and $\kappa_{\mathrm{e}} = 250.8 \pm 2.1$ kHz respectively, are fitted as described in the text.

We characterize our microwave resonator by recording its reflected response (both amplitude and phase) and fitting this with the equation[3]

$$R = \frac{(\kappa_{\mathrm{i}} - \kappa_{\mathrm{e}})/2 - i(\Delta - \omega_{\mathrm{c}})}{(\kappa_{\mathrm{i}} + \kappa_{\mathrm{e}})/2 - i(\Delta - \omega_{\mathrm{c}})}. \tag{11}$$

Here, the square of the reflection coefficient, $|R|^2$, describes the probability that a photon reflects off our cavity. Furthermore, the internal and external linewidths, κ_{i} and κ_{e}, sum up to the total linewidth $\kappa = \kappa_{\mathrm{i}} + \kappa_{\mathrm{e}}$, and the detuning $\Delta = \omega_{\mathrm{d}} - \omega_{\mathrm{c}}$ describes the difference between the drive frequency ω_{d} and the cavity center frequency ω_{c}.

We use a three-step fit process. First, we de-trend the cavity signal by fitting a polynomial of order 2 to the first and last 10% of the amplitude signal, and a polynomial of order 1 to the same parts of the phase signal. This assumes the cavity resonance is approximately at the center of our measurement span, and that the background is reasonably flat within this span. Then we fit an ellipse to the response R on a Smith chart, from which we compute the cavity parameters and use those as initial guesses for the third and final step. By using scipy's `curve_fit` function[8], we fit our data to Eq. (11). The response, fit and extracted parameters are shown in Supplementary Fig. 12. We fit the amplitude in logarithmic scale to enhance the accuracy around the cavity center, while the phase is fitted in linear scale.

Our cavity resonance frequency $\omega_{\mathrm{c}} = 2\pi\times 5.46180$ GHz, and the internal and external linewidths are $\kappa_{\mathrm{i}} = 2\pi\times 297.2\pm 2.8$ kHz and $\kappa_{\mathrm{e}} = 2\pi \times 250.8 \pm 2.1$ kHz respectively.

2. *Thermalization of drum motion*

We calibrate the temperature to which the mode of our mechanical resonator thermalizes by sweeping the temperature of the dilution refrigerator. At each temperature, we measure the mechanical spectrum and fit a Lorentzian to the data. This way, we can extract the frequency ω_m, linewidth γ_m, and the area of the mechanical peak.

The amplitude of the thermal motion peak is shown in Supplementary Fig. 13. It increases linearly with temperature below 200 mK. At higher temperatures the quasiparticles in the Al superconducting cavity shift and damp the cavity mode which reduce the readout efficiency. The peak amplitude stays proportional to the temperature all the way to the base temperature of 10 mK: we conclude that the drum thermalizes down to 10 mK and we use this assumption to extract g_0 in the next section.

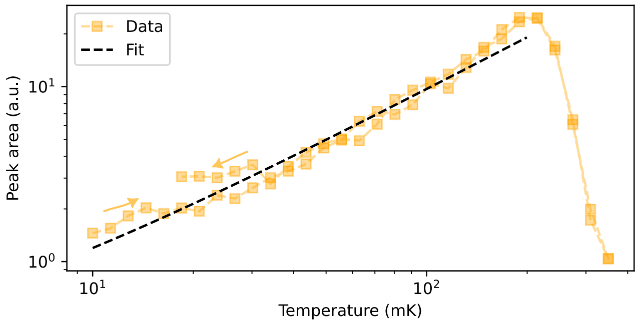

Supplementary Fig. 13 | Thermalization of the drum mode. Area of the fitted mechanical peaks, indicating the thermal energy of the oscillator mode. The dashed curve is a linear fit offset by only about 3 mK, well below the base temperature of 10 mK, showing the good thermalization of the mode with the cryostat at the base temperature. At higher temperatures, the microwave cavity response disappears, likely due to quasiparticles in the superconductor (Aluminium), which shifts the microwave cavity frequency.

3. *Calibration of single-photon coupling*

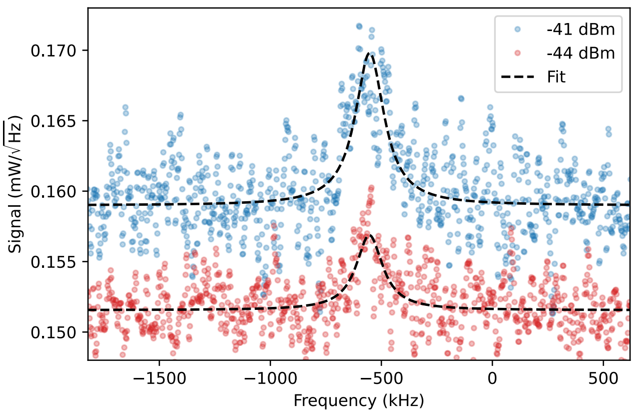

Supplementary Fig. 14 | Calibration of the optomechanical coupling rate. The amplitude of the scattered peak is compared to a signal of known power (not shown). The area under the peak is calculated from a Lorentzian fit, and the ratio of the fitted peak with the signal of known power yields the optomechanical coupling rate g_0.

The optomechanical coupling g_0 is calibrated by sending in a tone at the red sideband, $\omega_\mathrm{c} - \omega_\mathrm{m}$, and comparing the amplitude of the scattered peak with the amplitude of the drive. The resulting signal is shown in Supplementary Fig. 14, and we fit a Lorentzian curve to the peak. We extract the area A under the curve, which is proportional to the number of scattered photons, and we compare it to the number of photons in the drive tone, $\hat{a}^\dagger_\mathrm{sb}\hat{a}_\mathrm{sb}$. The optomechanical coupling can be extracted from these amplitudes as

$$g_0^2 = \frac{A}{|a_\mathrm{sb}|^2} \frac{|1 - \kappa_\mathrm{e}\chi(\omega_\mathrm{c} - \omega_\mathrm{m})|^2 |\chi(\omega_\mathrm{c} - \omega_\mathrm{m})|^2}{|\chi\omega_\mathrm{c}|^2 n_\mathrm{m}}, \tag{12}$$

which contains the ratio of the peak amplitude, as well as the cavity susceptibilities at the red sideband and cavity center (assuming zero detuning),

$$\begin{aligned} \chi(\omega_c - \omega_m) &= \frac{1}{\kappa/2 + i\omega_m} \\ \chi(\omega_c) &= \frac{1}{\kappa/2}. \end{aligned} \tag{13}$$

The thermal mechanical occupation can be calculated as

$$n_m = \frac{k_B T}{\hbar\omega_m}. \tag{14}$$

With these expressions, we fit $g_0 = 2\pi \times 150 \pm 9$ Hz.

4. *Effective linewidth*

We account for optical damping (sideband cooling) by using an effective linewidth, γ_{eff} that relates to the intrinsic (low-power) mechanical linewidth γ_m via

$$\gamma_{\text{eff}} = \gamma_m + \frac{4g_0^2|\alpha|^2}{\kappa} P = \gamma_m + \eta P. \tag{15}$$

Here, $|\alpha|^2$ is the number of photons in the cavity at the red sideband frequency, η is some coefficient which we are trying to fit and P is the power sent out from our microwave source at the red sideband frequency. The exact value of η depends not only on optomechanical parameters g_0 and κ, but also on the attenuation in the microwave lines between source and sample. However, as long as the latter are constant between measurements, we can use η and do not need to know the exact attenuation from our lines.

To fit the intrinsic linewidth, mechanical frequency and η, we vary the power sent in on the red sideband.

5. *Scale and phonon number calibration*

We do not know a priori the exact scaling between the spectral power that we measure and the expected spectral power of a single photon or phonon. Thus we need to derive an expression for the spectral power in terms of system parameters that can be measured, to use it as a fit function to our measurements.

Here we use operator formalism as the calibration described in this section is performed close to the quantum regime where vacuum fluctuations should be taken into account. We start from the equations of motion for the cavity field $\hat{a}$ and mechanical ladder operator $\hat{b}$ corresponding to $\tilde{x}$: $\tilde{x} = x_{\text{zpf}}(\hat{b} + \hat{b}^\dagger)$. In the sideband-resolved limit, with a drive detuned by $-\omega_m$ from the cavity frequency (at the red sideband), with $\hat{a}$ separated into a steady state amplitude and some fluctuations $\hat{a} = \alpha + \delta\hat{a}$, the equations of motion can be written in the frequency domain as

$$\begin{aligned} \hat{a}[\omega] &= \chi_c[\omega + \Delta]\left(-ig_0\alpha\left(\hat{b}[\omega] + \hat{b}^\dagger[\omega + 2\omega_m]\right) + \sqrt{\kappa_i}\hat{a}_{\text{in}}[\omega]\right), \\ \hat{b}[\omega] &= \chi_m[\omega]\left(-ig_0\left(\alpha^*\hat{a}[\omega] + \alpha\hat{a}^\dagger[\omega + 2\omega_m]\right) + \sqrt{\gamma_m}\hat{b}_{\text{in}}[\omega]\right). \end{aligned} \tag{16}$$

Here, the cavity susceptibility $\chi_c[\omega] = \frac{1}{\kappa/2 - i\omega}$ and the mechanical susceptibility $\chi_m[\omega] = \frac{1}{\gamma_m/2 - i\omega}$ are used as shorthands, and the input fields are $\hat{a}_{\text{in}}[\omega]$ and $\hat{b}_{\text{in}}[\omega]$.

In the good cavity limit, we can neglect the terms at $\omega \pm 2\omega_m$ and Δ. We can replace $\hat{b}[\omega]$ in our expression for $\hat{a}[\omega]$ and compute the spectrum S_{out} of the output field $\hat{a}_{\text{out}}[\omega] = \hat{a}_{\text{in}}[\omega] - \sqrt{\kappa_e}\hat{a}[\omega]$. We get

$$S_{\text{out}} = \frac{1}{2} + \kappa_e\kappa_i \left|\tilde{\chi}_c[\omega]\right|^2 n_{\text{cav}} + g_0^2|\alpha|^2\gamma_m\kappa_e \left|\tilde{\chi}_c[\omega]\chi_m[\omega]\right|^2 n_{\text{th}}. \tag{17}$$

The three terms come from the external port of the cavity (vacuum), environmental noise at the cavity frequency (n_{cav}) and mechanical noise (thermal, n_m). The shorthand $\tilde{\chi}_c[\omega] = \frac{\chi_c[\omega]}{1+g_0^2|\alpha|^2\chi_c[\omega]\chi_m[\omega]}$ denotes the cavity susceptibility that is modified due to

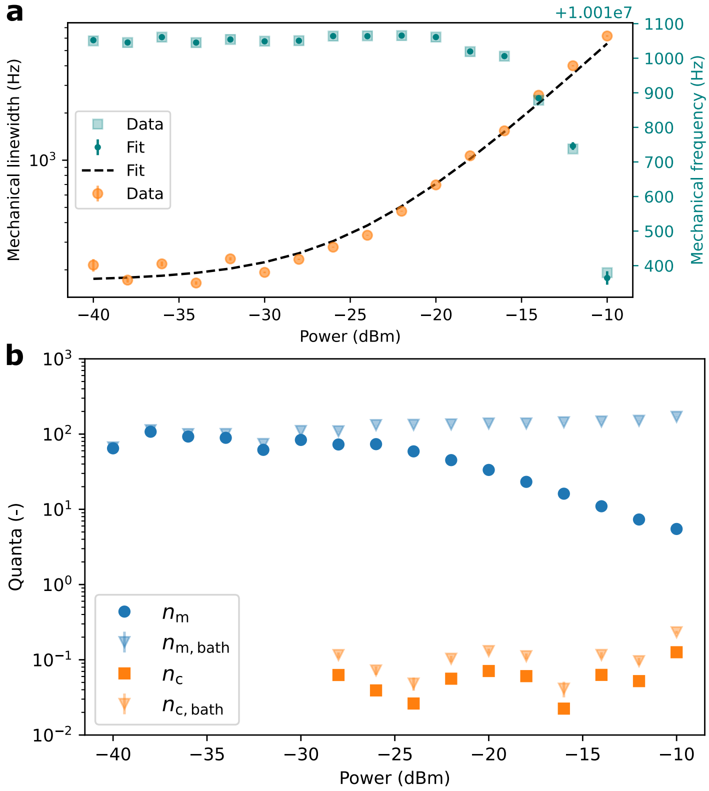

Supplementary Fig. 15 | Power calibration. a Mechanical linewidths (orange) and frequencies (teal) for various driving powers on the red sideband. **b** Extracted mechanical occupation n_{m} and cavity photon number n_{c}, as well as the equivalent quanta in the respective thermal baths.

the optomechanical interaction. In the fitting procedure, we subtract the constant offset, so the factor 1/2 in Eq. (17) disappears. Our final fit has the form $S_{\mathrm{fit}} = S_c \times (S_{\mathrm{out}}[\omega] - 1/2)$, and requires knowing $\kappa_{\mathrm{e}}, \kappa_{\mathrm{i}}, \gamma_{\mathrm{m}}, g_0, \alpha, n_{\mathrm{cav}}$, and n_{th} to extract our fit parameter, scale S_c. In favor of knowing α directly, we can use $g_0^2|\alpha|^2 = \frac{\kappa\eta P}{4}$ using the parameter η defined in Eq. (15).

The fit procedure is as follows: We assume that at sufficiently low red-detuned drive power, the mechanical occupation is unperturbed by the drive. For the points at the lowest powers shown in Supplementary Fig. 15a, below −32 dB, n_{m} is known from the reference temperature obtained from the thermalization step. Then we use the power-dependence parameter η obtained from the effective linewidth step, and fit the data at all powers to obtain n_{m} and n_{c} at each power. The effective linewidth is shown in Supplementary Fig. 15a, with intrinsic mechanical linewidth $\gamma_{\mathrm{m}} = 168.9 \pm 9.5$ Hz and power factor $\eta = 5.37 \cdot 10^4$ Hz mW^{-1} completing the fit.

With our initial guess of the occupation numbers, we subsequently refine the fits of our scale parameter and η (now using the whole dataset). Using the updated values, we re-fit n_{m} and n_{c} at all powers, and the final result is shown in Supplementary Fig. 15b. In the plots, we have used the final $\eta = 5.37 \cdot 10^4$ Hz mW^{-1}, and scale $S_c = 2.04 \cdot 10^{-15}\ \frac{\mathrm{W}/\sqrt{\mathrm{Hz}}}{n_{\mathrm{c}}}$.

D. Data filtering

Due to limitations of our vector network analyzer, we drive our system at a series of discrete frequencies instead of a continuous sweep. This way, we can control the step size and direction, which allows us to do a bidirectional measurement where the drive frequency first increases and then decreases. We record the response of our system on a separate spectrum analyzer (SA), which integrates for the full duration of the increasing/decreasing segments separately. The response measured at the second red sideband ($\omega_{\mathrm{c}} - 2\omega_{\mathrm{m}}$) during the upwards frequency sweep is shown in Supplementary Fig. 16a.

Our SA records the spectrum using a much finer set of points than the frequencies at which the vector network analyzer outputs its drive. This condition creates a periodic pattern of peaks in the SA-recorded spectrum, which obscures the true shape of the curve. We are only interested in the tops of the peaks, since there is no sideband drive at the frequencies between the peaks. We filter the SA points in a small bandwidth around each of the vector network analyzer output frequencies, and integrate

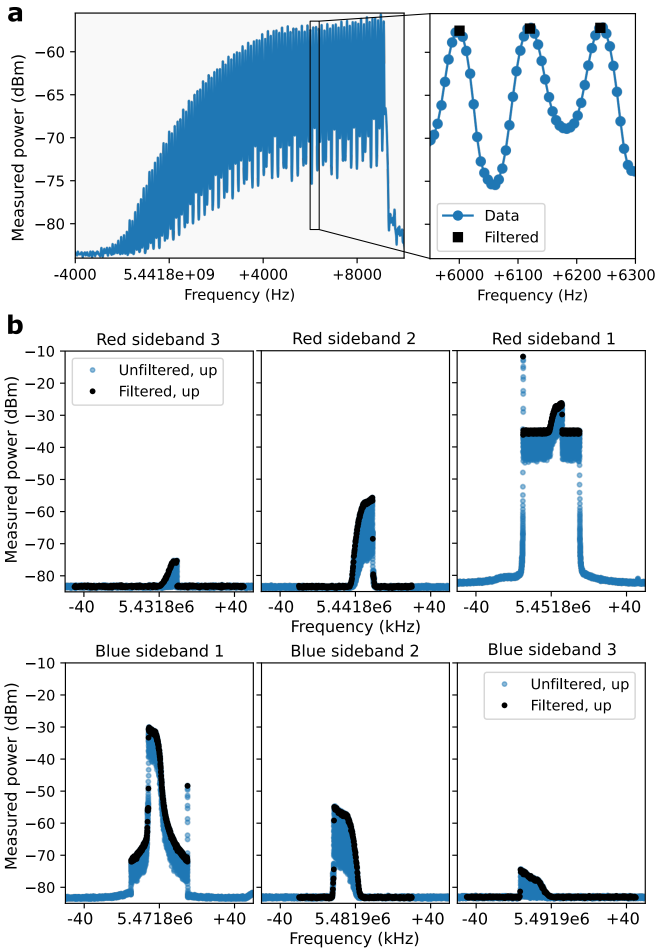

Supplementary Fig. 16 | Data filtering. a The measured power on the spectrum analyzer shows periodic peaks at the sideband drive frequency steps. We filter out the peaks located at these frequencies (black squares). **b** All sidebands as recorded on the spectrum analyzer (blue) and filtered (black). Clearly visible is the noise pedestal due to the drive at the first red sideband. The sharp peak at the edge of the pedestal is from the vector network analyzer start/stop frequency.

the power over that bandwidth. The filtered signal is a much shorter set of points that traces out the tops of the peaks. We have plotted the unfiltered data and the filtered signals respectively as blue dots and black squares in Supplementary Fig. 16a.

III. SUPPLEMENTARY DISCUSSIONS

A. Exclusion of other sources of nonlinearity

1. Electrostatic nonlinearity: Average potential offset

The top and bottom plates of our drum form a capacitance separated by a vacuum gap at equilibrium of $d' \simeq 15$ nm. Any static average potential difference between the plates exerts an attractive force between the plates, which has been used in a similar system to tune the vacuum gap[9]. In our system, the top and bottom plates are connected galvanically through the superconducting cavity, thus they are two sides of the same superconductor. In the absence of a large thermal gradient across our device, we expect the average potential difference between the plates to be negligibly small. Nonetheless, if there were a 1 V static average potential difference, this would correspond to a pressure of $P_{\mathrm{elec}} \simeq 150$ Pa for $d' = 15$ nm (based on a COMSOL simulation, as shown in Supplementary Fig. 17). This pressure is negligible compared to the Casimir pressure, which at this distance is $P_{\mathrm{c}} = 12.0 \pm 0.6$ kPa.

Our experiment is not directly sensitive to the absolute value of the (Casimir) pressure, and neither is it directly sensitive to any absolute pressure from the electrostatic force. It is sensitive to the *nonlinearity* that originates from these effects: The electrostatic force contributes a softening nonlinearity that scales with $P_{\mathrm{elec}} \propto d^{-2}$. This scaling is much weaker than the Casimir force scaling, $P_{\mathrm{c}} \propto d^{-3.2}$. Since the magnitude of the electrostatic force is much less and the nonlinearity scales much weaker than the Casimir force, the effect from the average potential difference is negligible.

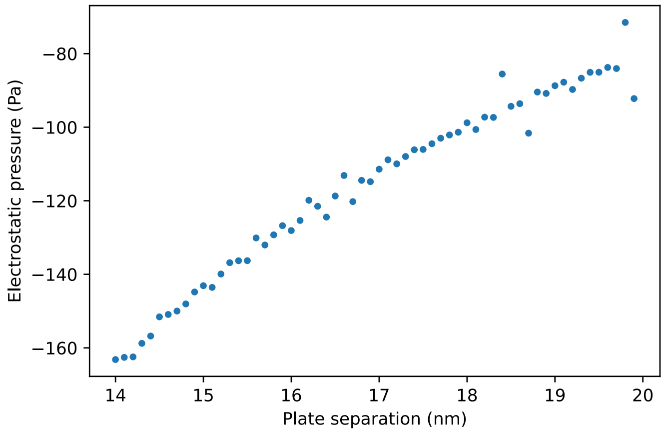

Supplementary Fig. 17 | Electrostatic effects. Electrostatic pressure due to a 1 V static potential offset between the drum plates, as a function of their separation distance d. Due to the small energies involved and the geometry of the simulation, it is sensitive to mesh-related inaccuracies.

2. Electrostatic nonlinearity: Potential patches

Crystal grain orientations can cause local differences in the electrostatic potential[10], also known as potential patches[11]. This means that although two closely spaced conductors may have the same *average* potential, there may still be a non-zero attractive electrostatic force between the conductors. Numerical simulations of randomized patch geometries can be used to estimate the force contributed by these potential patches[11–13]. Such numerical simulations rely on accurate information about the (lateral) sizes of these patches, as well as their voltage distribution[14,15].

We experimentally measure the patches in our aluminium to have a characteristic size of ℓ = 158 nm and a potential intensity that falls well within a normal distribution width σ = 100 mV. With these numbers, we overestimate the pressure exerted by potential patches by about a factor 10. Nonetheless, we find that the patch pressure is several orders of magnitude smaller than the Casimir pressure at our equilibrium position d' = 15.1 nm, as shown in Supplementary Fig. 18. We exclude that potential patches are responsible for the nonlinearity that we observe in our mechanical resonator. We describe the experimental details in the next paragraphs.

KPFM measurement of patches

We use Kelvin Probe Force Microscopy (KPFM) to locally measure the potential on our sample, which is a well-established technique based on a conductive atomic force microscope cantilever[16,17]. We use a sample that was fabricated in the same batch as the sample reported in the main paper. The KPFM measurement results are plotted in Supplementary Fig. 19, where we see characteristic aluminium spots where the potential is $\simeq$ 100 − 200 mV below the mean. This corresponds to the work function difference between the different crystalline orientations of aluminium: The work function of aluminium in the ⟨100⟩-direction is 4.20 eV, in the ⟨110⟩-direction it is 4.06 eV and in the ⟨111⟩-direction it is 4.26 eV[18]. There is no correlation between the potential and height, which are measured simultaneously.

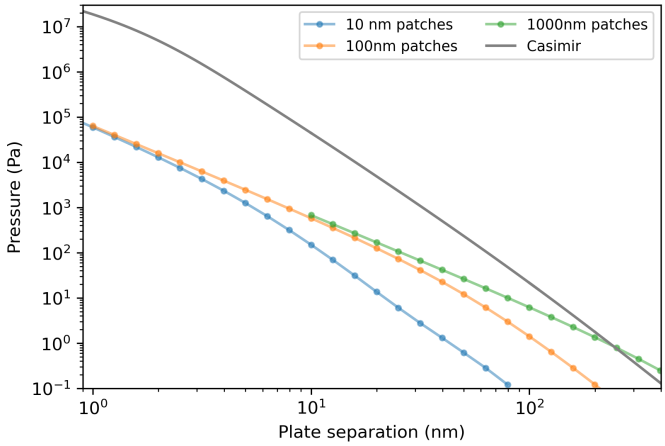

Supplementary Fig. 18 | Patch pressure. Calculated Casimir pressure and patch potential pressure for patches normally distributed with a standard deviation of 100 mV, for various patch sizes.

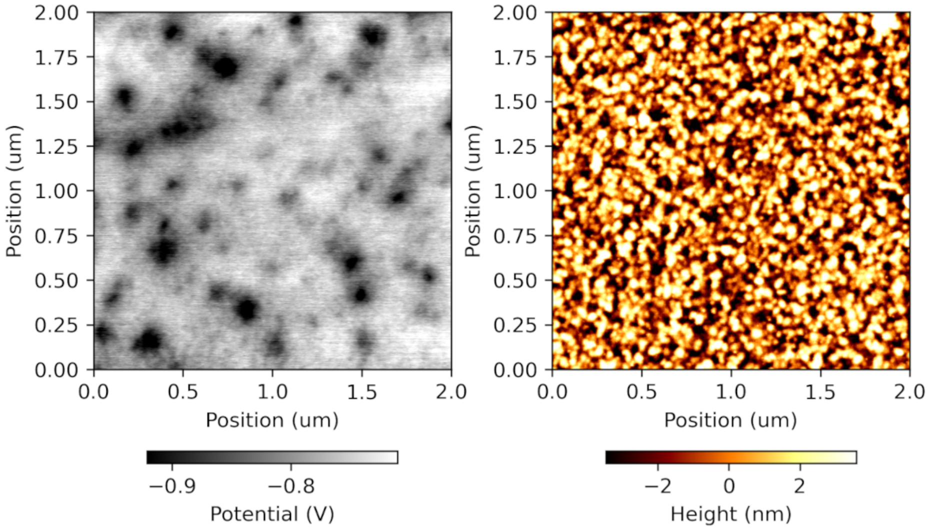

Supplementary Fig. 19 | Potential patches. Measured surface potential (left) and height (right) of a $2 \times 2\ \mu\mathrm{m}^2$ aluminium film from the same fabrication batch as the sample studied in the main text.

Patch strength

We expect a Gaussian distribution of the potentials, since the crystalline orientations should be random. But when we bin the measurement points of the potential, the Gaussian fit shown in Supplementary Fig. 20 is not a good fit. There is a distinct tail towards lower potentials, which represents the spots seen in Supplementary Fig. 19. The Gaussian fit is centered around a mean value −768 mV with a standard deviation σ of 30.4 mV. The mean potential seen in Supplementary Fig. 19 is due to the insulating substrate due to which the sampled area is not well galvanically connected to ground: Our KPFM tip touches down before the measurement and this transfers some charge to the sample. Any excess charge leaks out over time (timescale of approximately 30 minutes in air), so our measurement shows some offset potential.

Patch size

Besides the intensities of the potential patches, their spatial extent (average patch feature size ℓ) strongly affects the distance scaling of the electrostatic force they exert[12,13]. Recent simulations show that the lateral resolution of the KPFM probe can lead to an overestimation of the patch size and an underestimation of the patch intensity[19]. We use ASYELEC02 probes in our AFM, which have a nominal tip radius of 25 nm, and operate in tapping mode with an amplitude 10 nm. With these numbers, we can estimate the lateral resolution of our KPFM measurement using[20] $\ell_{\mathrm{min}} = \sqrt{RH} \simeq 16$ nm where R is the tip radius and H is the minimal tip-sample distance. We determine the average size of the experimentally measured patches using the `correlate2d`

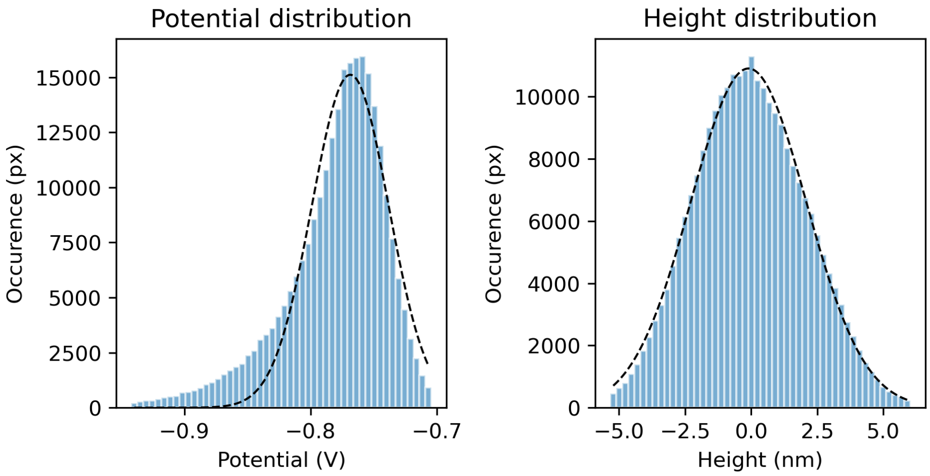

Supplementary Fig. 20 | Potential patch statistics. Distribution of the measured potentials and heights for the area shown in Supplementary Fig. 19, and Gaussian fits (dashed black lines).

function from Scipy, which is plotted in Supplementary Fig. 21. We find the average patch size ℓ_p is 158 nm, which is well above our minimal lateral resolution, $\ell_p \gg \ell_{min}$. Thus there is no reason to assume we significantly overestimate the characteristic patch size ℓ or underestimate the patch intensity distribution width σ. Our KPFM measurement also measures the height variation in our sample. The height is well-described by a Gaussian fit centered around −0.1 nm with a σ_h of 2.19 nm and a characteristic feature size ℓ_{height} = 32 nm, as shown in Supplementary Fig. 20.

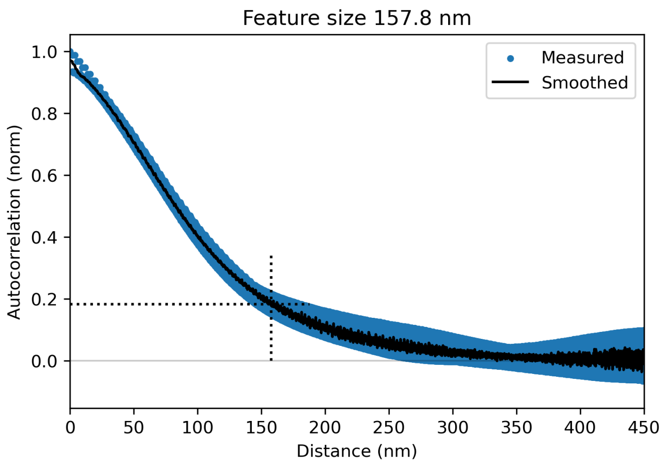

Supplementary Fig. 21 | Potential patch size. Autocorrelation of the potential shown in Supplementary Fig. 19. The average patch size ℓ_p is the distance at which the normalized autocorrelation drops to $1/2e \simeq 0.184$ (dotted lines), which is 157.8 nm for our aluminium film.

Patch textures reproducibility

Our patch characterization was performed on a sample that was processed identically (i.e., in the same batch) as the sample in which we measured the Casimir force. We have measured the patch statistics on 8 separate areas on the aluminium parts of the sample, and obtained similar patch intensities and patch sizes. The average patch intensity distribution width from all 8 areas σ_{mean} = 36 mV, and the average patch size is ℓ_{mean} = 160 nm, with both parameters varying minimally between different measurement areas.

While some processing steps greatly affect the size and intensity of potential patches[21], we have performed KPFM measurements on multiple samples (from different batches) and found our processing does not significantly affect the potential patches. The patch intensity does not appear affected by our release etch step, as we have measured σ_{mean} = 41 mV before release (σ_{mean} = 36 mV after). The heat treatment step has the largest effect on the patch intensity, σ_{mean} = 63 mV before any heat treatment, σ_{mean} = 55 mV after 15 minutes of 200 °C, σ_{mean} = 47 mV after 15 minutes of 240 °C, σ_{mean} = 42 mV after 15 minutes of 260 °C, and $\sigma_{\text{mean}} = 41$ mV after 15 minutes of 280 °C. These findings appear consistent with potential patches that originate solely from the crystalline structure of the material. Our patch measurements were performed on a sample that has been processed simultaneously and identically to the experimentally reported sample, so we consider them to be representative of the patches present in the drum we tested.

Estimate of patch forces

We calculate the effect of patches for our drum geometry using the simulation framework we developed in an earlier work[13]. We generate Voronoi patterns based on randomized patches of various sizes, with normally distributed potentials with a σ = 100 mV. Our patterns consist of 400 patches, and we compute the electrostatic energy. From the variation of energy with plate separation, we extract the pressure from the patch potentials for various plate separations as shown in Supplementary Fig. 18. We find the well-known limit behaviors with the patch size[11]: When $\ell \gg d$, $P_{\text{patch}} \propto d^{-2}$, while when $\ell \ll d$, $P_{\text{patch}} \propto d^{-4}$. The regime where $\ell \gg d$ leads to the greatest patch pressure in absolute sense, yet this is still several orders of magnitude smaller than the Casimir pressure for our plate separation $d = 15$ nm. We find $P_{\text{patch}} = 230$ Pa at a vacuum gap of 15 nm, much smaller than the Casimir pressure $P_{\text{c}} = 12000 \pm 600$ Pa, as shown in Supplementary Fig. 18. We note that in Casimir experiments at larger distances ($d \gtrsim 200$ nm), the Casimir pressure can be comparable in amplitude to the patch pressure.

3. *Mechanical nonlinearity: Geometric origin*

There is a significant body of literature on the mechanical nonlinearities with a purely geometric origin. In our experimental platform of superconducting Aluminium drum resonators, Supplementary Ref. 22 provides an excellent theoretical background that is experimentally tested in Supplementary Ref. 23. The nonlinearity due to geometry is a *hardening* nonlinearity in these drum resonators, both on theoretical grounds and experimental evidence[22,23]. The Casimir force contributes a *softening* nonlinearity, which is exactly what is described in the main text, and thus we exclude the geometric nonlinearity on qualitative grounds.

Furthermore, we can exclude the geometric mechanical nonlinearity on quantitative grounds. We follow the method of Supplementary Ref. 22, which is based on Kirchhoff-Love theory for circular membranes. The first assumption in this method is that the resonator is essentially a 2D circular membrane with coordinates (r, θ), which has modes purely moving in the out-of-plane z direction. From COMSOL simulations, we verify that the mode shown in Fig. 8b of the Methods consists for > 99% of motion in the z-direction. Thus we separate the variables of the function $f_{n,m}$ describing the motion of our structure for the (n, m) mode,

$$f_{n,m}(r, \theta, t) = z_{n,m}(t)\psi_{n,m}(r, \theta). \tag{18}$$

The part $z_{n,m}(t)$ describes the oscillating motion, and $\psi_{n,m}(r, \theta)$ is the normalized mode shape. The mass and stiffness parameters of the fundamental mode (which is the one we study) are given as[22]

$$\begin{aligned}
\mathcal{M}_{0,0} &= \rho h \int_0^{2\pi} \int_0^{R_{\text{d}}} \left(\psi_{0,0}(r, \theta)\right)^2 r dr d\theta, \\
\mathcal{K}_{0,0} &= \frac{1}{12} \frac{E h^3}{1 - \nu_{\text{r}}^2} \int_0^{2\pi} \int_0^{R_{\text{d}}} \left(\psi_{0,0}(r, \theta)\Delta^2 \psi_{0,0}(r, \theta)\right) r dr d\theta \\
&\quad + h\sigma_0 \int_0^{2\pi} \int_0^{R_{\text{d}}} \left(\psi_{0,0}(r, \theta)\Delta \psi_{0,0}(r, \theta)\right) r dr d\theta.
\end{aligned} \tag{19}$$

We denote the material parameters: ρ is the density of the drum material, E is the Young's modulus, ν_{r} the Poisson's ratio, and σ_0 the stress (negative for tensile stress). The drum geometry is taken into account via the drum radius R_{d} and thickness h. Finally,

$$\Delta\ldots = \frac{1}{r}\frac{\partial\ldots}{\partial r}\left(r\frac{\partial\ldots}{\partial r}\right) + \frac{1}{r^2}\frac{\partial^2\ldots}{\partial\theta^2} \tag{20}$$

is the Laplacian operator in polar coordinates. From Eq. (19), we can calculate the mode frequency $\omega_{0,0} = \sqrt{\mathcal{K}_{0,0}/\mathcal{M}_{0,0}}$.

In the COMSOL model shown in Fig. 8 of Methods, we use material parameters $\rho = 2700\ \text{kg}\,\text{m}^{-3}$, $E = 76.6$ GPa, $\nu_{\text{r}} = 0.32$, and the average value of the von Mises stress over the drum domain, $\sigma_0 = -270$ MPa (following the convention of Supplementary Ref. 22, tensile stress is negative in the analytical description, while in the COMSOL plots tensile stress is positive). Combined with the drum diameter $2R_{\text{d}} = 11.3$ µm and the thickness of the evaporated Al $h = 120$ nm, we can evaluate Eq. (19). We find $\mathcal{M}_{0,0} = 1.38 \times 10^{-13}\ \text{kg}\,\text{m}^2$ and $\mathcal{K}_{0,0} = 1467\ \text{N}\,\text{m}$. The resulting frequency $\omega_{0,0} = 2\pi \times 16.4$ MHz is close to our bare resonator frequency $\omega_{\text{r}} = 2\pi \times 16.3$ MHz.

The geometric nonlinearity can be captured in a cubic term ($\propto x^3$), and its coefficient for the fundamental mode can be found from the expression[22]

$$\tilde{\mathcal{K}}_{0,0} = -\frac{Eh}{R_{\mathrm{d}}^2}\frac{C_{0,0}^{(1)}}{1-\nu_{\mathrm{r}}}\int_0^{2\pi}\int_0^{R_{\mathrm{d}}}(\psi_{0,0}(r,\theta)\Delta\psi_{0,0}(r,\theta))\,rdrd\theta \tag{21}$$

where $C_{0,0}^{(1)} = 0.389664$ as tabulated in Table IV of Supplementary Ref. 22. From our COMSOL simulations, we obtain $\tilde{\mathcal{K}}_{0,0} = 3.55\times10^{15}\ \mathrm{N\,m^{-1}}$. We then relate this to the coefficient α_{D} of the Duffing term,

$$\ddot{x} + \gamma_{\mathrm{r}}\dot{x} + \omega_{\mathrm{r}}x + \alpha_{\mathrm{D}}x^3 = \frac{F_{\mathrm{d}}}{m_{\mathrm{eff}}}, \tag{22}$$

where $\alpha_{\mathrm{D}} = \tilde{\mathcal{K}}_{0,0}/\mathcal{M}_{0,0} = +2.57\times10^{28}\ \mathrm{m^{-2}\,s^{-2}}$. This value is close to the experimental fit of Refs. 22 and 23, which is $\alpha_{\mathrm{D}} = +7\times10^{27}\ \mathrm{m^{-2}\,s^{-2}}$ in a drum resonator that is of nearly identical design to the one in this work.

From the coefficient α_{D}, we can estimate that a +1 Hz frequency shift should occur if the motional amplitude is $x \simeq 0.6$ nm. At those amplitudes, we see a multiple-kHz *negative* frequency shift corresponding to the Casimir force. Thus we can exclude the geometrical mechanical nonlinearity based on the magnitude and sign of the frequency shift.

4. *Higher-order optomechanical couplings*

The optomechanical cavity is formed by a plate capacitor where one of the plates is mechanically compliant. The capacitance is not a linear function of the separation distance d', and g_0 only represents the first-order Taylor series of the capacitance in x/d'. To estimate the 'higher order' optomechanical couplings that stem from the nonlinearity of the capacitance expansion, we follow the method of[23] derived for the same type of system. The cavity frequency and couplings up to third order in x are

$$\begin{aligned}
\omega_{\mathrm{c}}(x) &= \omega_{\mathrm{c}}(0) - \left[g_0\frac{x}{x_{\mathrm{zpf}}} + \frac{g_1}{2}\left(\frac{x}{x_{\mathrm{zpf}}}\right)^2 + \frac{g_2}{2}\left(\frac{x}{x_{\mathrm{zpf}}}\right)^3\right]\\
g_1 &= g_0\left[2\frac{x_{\mathrm{zpf}}}{d'} - 3\frac{g_0}{\omega_{\mathrm{c}}(0)}\right]\\
g_2 &= g_0\left[2\left(\frac{x_{\mathrm{zpf}}}{d'}\right)^2 - 6\frac{x_{\mathrm{zpf}}}{d'}\frac{g_0}{\omega_{\mathrm{c}}(0)} + 5\left(\frac{g_0}{\omega_{\mathrm{c}}(0)}\right)^2\right]
\end{aligned} \tag{23}$$

For a motion amplitude of $x = 0.2$ nm, close to the maximum amplitude observed here, the frequency shift from the g_0 term is $\Delta\omega_{\mathrm{c}} \simeq -6.5$ MHz, the additional shift from g_1 would be $\Delta\omega_{\mathrm{c}} = -7.5\times10^{-2}$ MHz and the additional shift from g_2 would be $\Delta\omega_{\mathrm{c}} = -8.7\times10^{-4}$ MHz. These higher-order contributions are only a relevant contribution to the frequency shift for extremely large displacements ($\simeq$ nm). At these displacements, the frequency shift is much larger than the cavity linewidth, $\Delta\omega_{\mathrm{c}} \gg \kappa$, so the drive efficiency that we describe in the main text is the most important optomechanical effect to take into account. We emphasize that the nonlinearity from the plate capacitor expansion only affects the *cavity* frequency shift and not the mechanical frequency shift from the Casimir force.

B. Measurements on a second device

We have repeated the experiments of the main text in a second device, fabricated using an identical design but in a different fabrication run. The parameters of the device were characterized using the same method as for the device in the main text, and they are reported in Supplementary Table 1.

In the absence of the Casimir force, the devices have a similar mechanical resonance frequency. However, this second device has a slightly different separation of the plates at mechanical zero (d), the final mechanical frequency is rather different due to the nonlinear nature of the Casimir force. Due to the lower optomechanical coupling rate, and higher cavity linewidth, it requires more drive power to reach larger displacement amplitudes, and we are limited by the maximum power that our measurement chain can handle. These measurements were performed in a different dilution refrigerator to the experiments in the main text, with a separate set of measurement equipment.

One of the mechanical response curves of the second device is shown in Supplementary Fig. 22. We have performed the same calibration procedure as in the device of the main text, and extract $d = 19.1 \pm 0.5$ nm (solid black line) from a fit to the data. For completeness, we also show the theory curves for $d = 19.6$ nm (dotted black line) and $d = 18.6$ nm (dashed black line).

Quantity	Symbol	Value
Unperturbed frequency	ω_r	$2\pi \times 16.710$ MHz
Mechanical frequency	ω_m	$2\pi \times 13.688$ MHz
Mechanical linewidth	$\gamma_r \simeq \gamma_m$	$2\pi \times 231 \pm 4$ Hz
Cavity frequency	ω_c	$2\pi \times 7.589718$ GHz
External linewidth	κ_e	$2\pi \times 304.7 \pm 2.8$ kHz
Internal linewidth	κ_i	$2\pi \times 608.7 \pm 6.2$ kHz
Optomechanical coupling	g_0	$2\pi \times 67 \pm 3$ Hz
Effective mass	m_{eff}	3.96×10^{-14} kg
Rest separation without Cas. f.	d	19.1 ± 0.5 nm
Rest separation	d'	17.3 ± 0.5 nm
Bottom plate diameter	$2r$	11.3 µm
Casimir amplitude	P	$(1275 \pm 7) \cdot 10^{-24}$ Pa m^n
Casimir force scaling exponent	n	3.193

Supplementary Table 1 | Parameters of the second device.

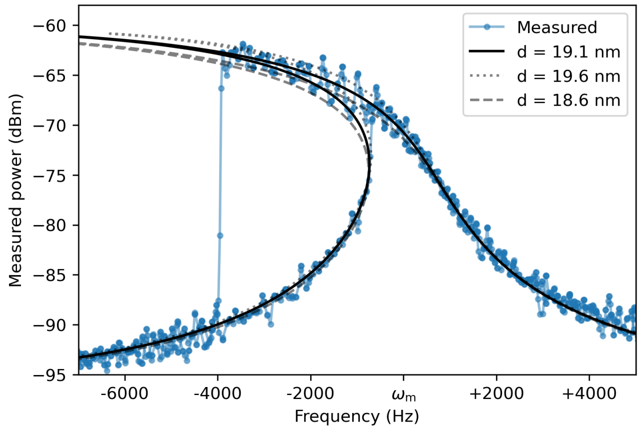

Supplementary Fig. 22 | Measurement of the nonlinearity in a second device. The measured response (blue) for 10 dBm cavity drive power and 0 dBm red sideband drive power. The theory curves based on the Casimir force for a separation of mechanical zero of d = 19.1 nm (solid black line), d = 19.6 nm (dotted black line) and d = 18.6 nm (dashed black line) are overlaid on the measured data. The d = 19.1 nm curve is closest to the center of the measured data.

SUPPLEMENTARY REFERENCES

[1] E. M. Lifshitz, The theory of molecular attractive forces between solids, Journal of Experimental and Theoretical Physics **2**, 73 (1956).
[2] G. Palasantzas, P. J. van Zwol, and J. T. M. de Hosson, Transition from casimir to van der waals force between macroscopic bodies, Applied Physics Letters **93**, 121912 (2008).
[3] M. Aspelmeyer, T. J. Kippenberg, and F. Marquardt, Cavity optomechanics, Reviews of Modern Physics **86**, 1391 (2014).
[4] T. J. Kippenberg and K. J. Vahala, Cavity opto-mechanics, Optics Express **15**, 17172 (2007).
[5] B. He, Q. Lin, M. Orszag, and M. Xiao, Mechanical oscillations frozen on discrete levels by two optical driving fields, Physical Review A **102**, 011503 (2020).
[6] E. D. Palik, ed., *Handbook of optical constants of solids*, Vol. 1 (Academic, New York, 1997).
[7] L. Mercier de Lépinay, C. F. Ockeloen-Korppi, M. J. Woolley, and M. A. Sillanpää, Quantummechanics-free subsystem with mechanical oscillators, Science **372**, 625 (2021).
[8] P. Virtanen, R. Gommers, T. E. Oliphant, M. Haberland, T. Reddy, D. Cournapeau, E. Burovski, P. Peterson, W. Weckesser, J. Bright, S. J. van der Walt, M. Brett, J. Wilson, K. Jarrod Millman, N. Mayorov, A. R. J. Nelson, E. Jones, R. Kern, E. Larson, C. J. Carey, I. Polat, Y. Feng, E. W. Moore, J. VanderPlas, D. Laxalde, J. Perktold, R. Cimrman, I. Hendriksen, E. A. Quintero, C. R. Harris, A. M. Archibald, A. H. Ribeiro, F. Pedregosa, P. van Mulbregt, and Scipy 1.0 Contributors, Scipy 1.0: fundamental algorithms for scientific computing in Python, Nature Methods **17**, 261 (2020).
[9] R. W. Andrews, A. P. Reed, K. Cicak, J. D. Teufel, and K. W. Lehnert, Quantum-enabled temporal and spectral mode conversion of microwave signals, Nature Communications **6**, 10021 (2015).

[10] J. B. Camp, T. W. Darling, and R. E. Brown, Macroscopic variations of surface potentials of conductors, Journal of Applied Physics **69**, 7126 (1991).

[11] C. C. Speake and C. Trenkel, Forces between superconducting surfaces due to spatial variations of surface potential, Physical Review Letters **90**, 160403 (2003).

[12] J. Ke, W.-C. Dong, S.-H. Huang, Y.-J. Tan, W.-H. Tan, S.-Q. Yang, C.-G. Shao, and J. Luo, Electrostatic effect due to patch potentials between closely spaced surfaces, Physical Review D **107**, 065009 (2023).

[13] M. H. J. de Jong and L. Mercier de Lépinay, Simulating the electrostatic patch force in sphere-plate and plate-plate geometries, https://arxiv.org/abs/2408.16323 (2024), arxiv preprint.

[14] R. O. Behunin, F. Intravaia, D. A. R. Dalvit, P. A. Maia Neto, and S. Reynaud, Modeling electrostatic patch effects in Casimir force measurements, Physical Review A **85**, 012504 (2012).

[15] R. O. Behunin, Y. Zeng, D. A. R. Dalvit, and S. Reynaud, Electrostatic patch effects in Casimir-force experiments performed in sphere-plane geometry, Physical Review A **86**, 052509 (2012).

[16] R. O. Behunin, D. A. R. Dalvit, R. S. Decca, and C. C. Speake, Limits on the accuracy of force sensing at short separations due to patch potentials, Physical Review D **89**, 051301 (2014).

[17] J. L. Garrett, D. Somers, and J. N. Munday, The effect of patch potentials in Casimir force measurements determined by heterodyne Kelvin probe force microscopy, Journal of Physics: Condensed Matter **27**, 214012 (2015).

[18] W. M. Haynes, ed., *CRC Handbook of Chemistry and Physics*, 96th ed. (CRC Press, Roca Baton, 2015).

[19] K. Shi, P. Luo, J. Liu, H. Yin, and Z. Zhou, Dependence of electrostatic patch force evaluation on the lateral resolution of Kelvin probe force microscopy, https://arxiv.org/abs/2411.01733 (2024), arxiv preprint.

[20] G. Lévêque, P. Cadet, and A. Arinero, Sensitivity and resolution in noncontact electrostatic force microscopy in the case of a constant potential, Physical Review B **71**, 205419 (2005).

[21] J. L. Garrett, J. Kim, and J. N. Munday, Measuring the effect of electrostatic patch potentials in Casimir force experiments, Physical Review Research **2**, 023355 (2020).

[22] D. Cattiaux, S. Kumar, X. Zhou, A. Fefferman, and E. Collin, Geometrical nonlinearity of circular plates and membranes: An alternative method, Journal of Applied Physics **128**, 104501 (2020).

[23] D. Cattiaux, X. Zhou, S. Kumar, I. Golokolenov, R. R. Gazizulin, A. Luck, L. Mercier de Lépinay, M. Sillanpää, A. D. Armour, A. Fefferman, and E. Collin, Beyond linear coupling in microwave optomechanics, Physical Review Research **2**, 033480 (2020).